Chapter 1 Halide Perovskites for Photonics: Recent History and Perspectives

CHAPTER

1 HALIDE PEROVSKITES FOR PHOTONICS: RECENT HISTORY AND PERSPECTIVES

Anna Vinattieri and Giacomo Giorgi

Vinattieri, A. and Giorgi, G., "Halide perovskites for photonics: Recent history and perspectives" in *Halide Perovskites for Photonics*, edited by A. Vinattieri and G. Giorgi (AIP Publishing, Melville, New York, 2021), pp. 1-1–1-28.

1.1 INTRODUCTION

Since the revolution introduced by bandgap engineering in the last decades of the past century [see the work of Capasso (1987) for a complete review], a link has been created between the community of material scientists (physicists and chemists) and the engineers mostly interested in technological developments. The possibility of designing a material with *a priori* definition of its properties (optical, electrical, mechanical, etc.) has opened the route to the dramatic innovation and impact that materials science and device technology have generated on society. The last decades of the 20th century can be considered as the *era* of epitaxially grown semiconductors with the undoubted advantage of a high crystalline quality of the grown material regardless of the highly expensive technique (Capper *et al.*, 2017). Recently, the ability of realizing high-quality semiconductor materials through solution-based techniques has rapidly driven the focus of research on halide perovskites (HPs) (Xing *et al.*, 2014). In fact, the ease and low-cost chemical growth/deposition, the control of the material bandgap by fine tuning the stoichiometry, and the possibility of realizing several types of nanostructures have made HPs among the most interesting classes of semiconductors for innovative devices (Huang *et al.*, 2018).

HPs have a chemical stoichiometry ABX_3. The X-site anion is a halide (mainly Cl, Br, and I), which plays a major direct role in determining the bandgap of the halide perovskite. The A-site cation can be an organic one such as methylammonium ($MA = CH_3NH_3^+$), formamidinium [$FA = {}^+HC(NH_2)_2$], or guanidinium [$GA = {}^+C(NH_2)_3$], with the latter forming alloys with other cations (Giorgi *et al.*, 2015; Giorgi and Yamashita, 2015a; De Marco *et al.*, 2016; Jodlowski *et al.*, 2017; and Wu *et al.*, 2019); it can also be an inorganic cation, mainly a group I alkali metal (Cs and Rb). The B-site cation is usually Pb

https://doi.org/10.1063/9780735423633_001 1-1
Halide Perovskites for Photonics, Anna Vinattieri and Giacomo Giorgi

(the archetypal compound of such a class is represented by $MAPbI_3$, hereafter also MAPI) even if Sn and Ge (Mg to a lesser extent) are under study for the production of *eco*-friendly HPs. In this sense, other perovskites, namely halide double perovskites with stoichiometry $A_2B'B''X_6$ (Palummo *et al.*, 2020a), both hybrid (Giorgi and Yamashita, 2015b) and full-inorganic (Slavney *et al.*, 2016; Volonakis *et al.*, 2017; Giorgi *et al.*, 2018; Wu *et al.*, 2018; and Palummo *et al.*, 2020b), are obtained by aliovalently replacing Pb pairs with couples of +1/+3 metals and have been reported to have improved properties in terms of stability.

Even though the first synthesis of an HP by Wells (1893) dates back to 1893, and then only recognized as a perovskite in 1957 by Møller (1957, 1958), HPs have been *rediscovered*, both in hybrid organic–inorganic HPs (OIHPs) and in the full-inorganic forms [David Mitzi, in the mid-1990s (Mitzi *et al.*, 1994; and Mitzi, 1999, 2001), was already paying close attention to two-dimensional (2D) systems], after the work of Miyasaka *et al.* (Kojima *et al.*, 2009), who at first used three-dimensional (3D) bulk $MAPbX_3$ (X = Br, I) as a light harvester in solar devices, exploiting the unique features that such a class of materials embodies in a single compound, i.e., an exceptional diffusion length of the carriers (Xing *et al.*, 2013; Stranks *et al.*, 2013; and Du, 2014), a bandgap very close to ideal for single-junction devices (Baikie *et al.*, 2013), and a symmetrical (ambipolar) behavior of the carrier effective masses (Lee *et al.*, 2012; Heo *et al.*, 2013; Giorgi *et al.*, 2013; and Giorgi and Yamashita, 2015c). Stability issues ascribed to the presence of a short-chain organic cation, being a strong limitation for device implementation, have somehow oriented the interest of the scientific community toward full-inorganic HPs, and especially toward $CsPbI_3$ [see the work of Shi *et al.* (2019) for a complete review], which nowadays finds similar application both in optoelectronics and in photonics (Song *et al.*, 2015; Li *et al.*, 2016; Su *et al.*, 2017; Tang *et al.*, 2017; and Zhang *et al.*, 2017). As direct bandgap semiconductors, the field of photonics takes great advantage of their unique features, and significant advancements in the last decade have been demonstrated with the realization of novel tools for applications in photovoltaics (PV), light emission, sensing, signal processing, etc. (Chen *et al.*, 2015; Sutherland and Sargent, 2016; Schönemann *et al.*, 2017; Ferrando *et al.*, 2018; Berestennikov *et al.*, 2019; Jena *et al.*, 2019; Makarov *et al.*, 2019; Liu *et al.*, 2020; and Zhao *et al.*, 2020).

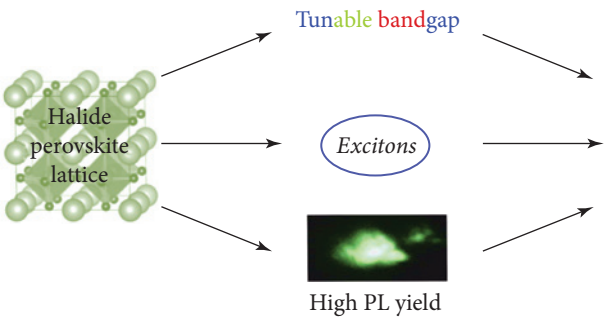

FIG. 1.1
Main properties of halide perovskites for photonics.

In Fig. 1.1, the main characteristics of the HPs of interest for photonics are summarized. The tunable bandgap, the significant excitonic features up to room temperature (RT), and the high photoluminescence (PL) efficiency represent the foundation for the development of photonic devices. If we focus on light generation, both incoherent and coherent, $CsPbBr_3$ has been proven to be a valid substitute for InGaN, given the similar value of the bandgap (~2.4 eV at RT) of interest for

efficient green emission but with much higher defect tolerance (Kang and Wang, 2017). In this way, a solution to the *green-gap* problem (Tong *et al.*, 2018), which has been widely debated, seems to have been found. Less investigated is $CsPbCl_3$, with a bandgap of ~3.1 eV at RT (Protesescu *et al.*, 2015), which is therefore the most suitable for the realization of white light-emitting diodes (LEDs) in combination with $CsPbX_3$ (X = Br, I) (Yoon *et al.*, 2016; and Yao *et al.*, 2017) and for the development of photonic structures in the blue spectral range.

One of the most interesting peculiarities of HPs is the control of material morphology by synthesis/deposition techniques: bulk and different kinds of nanostructures can be realized. Furthermore, light-induced self-assembly was recently demonstrated (Liu *et al.*, 2019), which opens the way to post-growth modification of the material nanostructure. Depending on the envisaged application, control of the material assembly constitutes a powerful tool for the optimal design of a device. In Fig. 1.2, the most common nanostructures are indicated with the specific applications for light emission.

In recent years, the integration of HPs in hybrid structures for photonics (see Fig. 1.3) has become a frontier research field; in fact, the possibility of combining the consolidated experience in silicon photonics with HP nanostructures (Gonzalez-Rodriguez *et al.*, 2016; Tiguntseva *et al.*, 2017; Furasova *et al.*, 2018; Rocks *et al.*, 2018; and Giorgi 2020), the use of plasmonic coupling, and the realization of perovskite metasurfaces have opened a wide possibility, which is highly promising for the development of innovative devices (Zhang *et al.*, 2019a).

The most commonly used techniques for the synthesis/deposition of halide perovskites on several kinds of substrates (dielectrics, semiconductors, metals, etc.), such as spin-coating and dipping, make possible the integration in photonics structures. Recently, sputtering has been demonstrated to be a powerful technique for the deposition of nanometric films of inorganic HPs on a large variety of

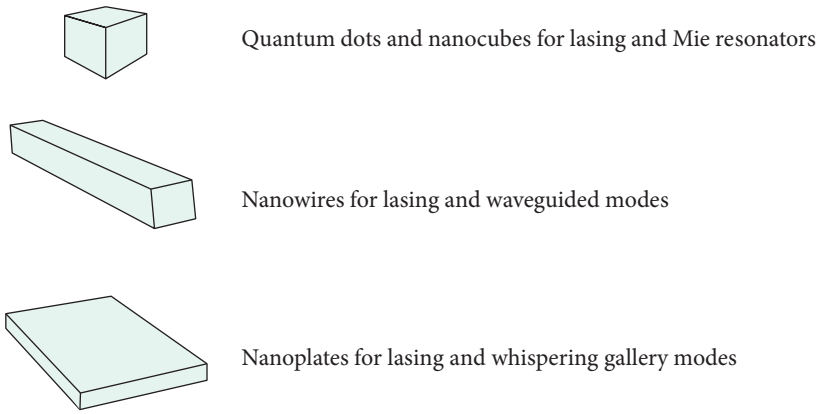

FIG. 1.2
Typical nanostructures of halide perovskites and corresponding application as light-emitting devices.

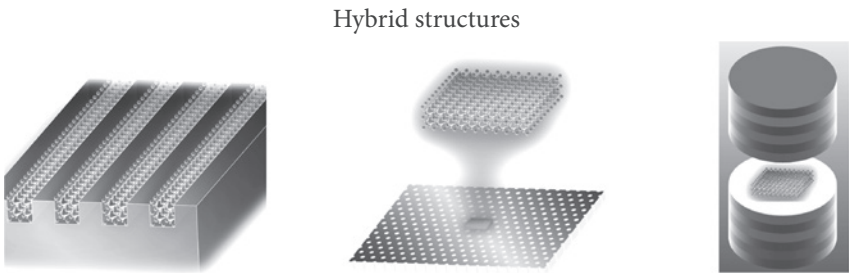

FIG. 1.3
Hybrid structures for photonics with halide perovskites.

substrates with a reduced surface roughness and a controlled deposition thickness between 50 and 500 nm. Moreover, samples prepared by sputtering show superior performance in terms of stability even in the absence of post-growth treatments (Borri *et al.*, 2020; and Falsini *et al.*, 2021). With this technique, multilayer deposition will become a much easier task with deposition control at the nanoscale, which is of relevance for device fabrication.

In this introductory chapter, we will focus on a few of the several experimental and theoretical aspects concerning the application of HPs to photonics.

1.2 AMPLIFIED SPONTANEOUS EMISSION AND LASING IN BULK AND NANOSTRUCTURES: EXPERIMENTS

One of the most interesting aspects concerning light emission in HPs is the possibility of a transition from an incoherent light-emission regime, i.e., photoluminescence or electroluminescence, to a coherent regime which is revealed by amplified spontaneous emission (ASE) and lasing. The main signatures of such a transition are a narrowing of the emission linewidth with the appearance of a modal structure and a decrease of the radiative lifetime when the excitation density exceeds a threshold value.

Initially, ASE and lasing were reported in $MAPX_3$ (X = Cl, Br, I) films and wires (Xing *et al.*, 2014; and Zhu *et al.*, 2015), which demonstrated that the long carrier lifetime, the high PL yield, the robustness to defects, and the slow Auger recombination make HPs a valid alternative to traditional semiconductors (e.g., III–V, II–VI, and nitrides) for the development of lasers both at the micrometer and nanometer scales. Later, to improve the material stability, inorganic HPs, in particular $CsPbBr_3$ and $CsPbI_3$, were considered. To the best of our knowledge, the use of $CsPbCl_3$ for lasing in the blue spectral region has been scarcely explored (Kondo *et al.*, 2005).

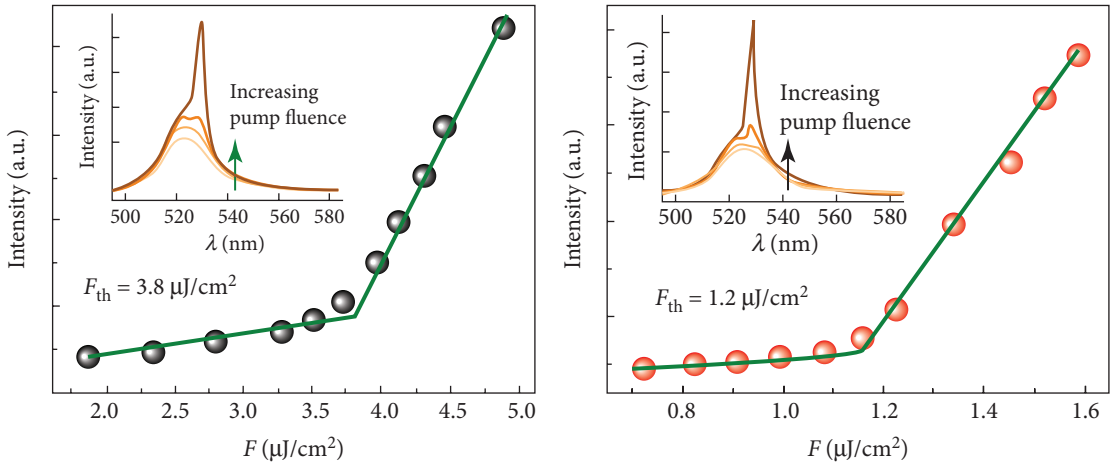

FIG. 1.4
Integrated emission intensity vs pump fluence in as-synthesized (left) and $PbBr_2$-treated $CsPbBr_3$ QD films (right). Adapted with permission Wang, Y. *et al.*, Nano Lett. **18**(8), 4976–4984 (2018b). Copyright 2018 American Chemical Society.

In Fig. 1.4, typical results of the transition from incoherent (PL) and coherent (lasing) emission is shown for $CsPbBr_3$ quantum dots prepared with and without a surface treatment (Wang *et al.*, 2018b). The appearance of a modal structure in the luminescence spectrum goes with a speeding up of the recombination dynamics which typically turns out to be resolution limited (Biccari *et al.*, 2017).

It is relevant to remark that the onset of a coherent regime can have a different origin depending on the material morphology. Typical examples are reported in Fig. 1.5, where several modes are observed above a threshold in the PL of a spin-coated MAPI film (left); the modes are usually unstable and change with time, while one/two modes are observed in a MAPI microwire (right).

To gain insights into the different behavior, polarization measurements can be helpful; in fact, no polarization is found for the *random* modes of the disordered sample, as expected for a random lasing condition, while in the presence of a sample structure with smooth surfaces acting itself as a cavity, strong polarization is detected. An example is provided in Fig. 1.6; in this case, no polarization is found with no change below and above the threshold for a MAPI spin-coated film [Fig. 1.6(a)], while two orthogonally polarized modes, which correspond to a lasing occurring between the two orthogonal axes of the rectangular wire, are detected in a MAPI microwire [Figs. 1.6(b)–1.6(d)].

The morphology of the perovskite structure clearly plays a major role in determining the occurrence of a coherent regime for the emission (Zhang *et al.*, 2019b). As illustrated in Fig. 1.2, the different morphologies of the HP nanostructures, which are highly controllable by the selection of fabrication protocols, allow us to explore several configurations for photonic applications. Quantum dots/nanoparticles, being light-emitting subwavelength nanostructures, in consideration of the high

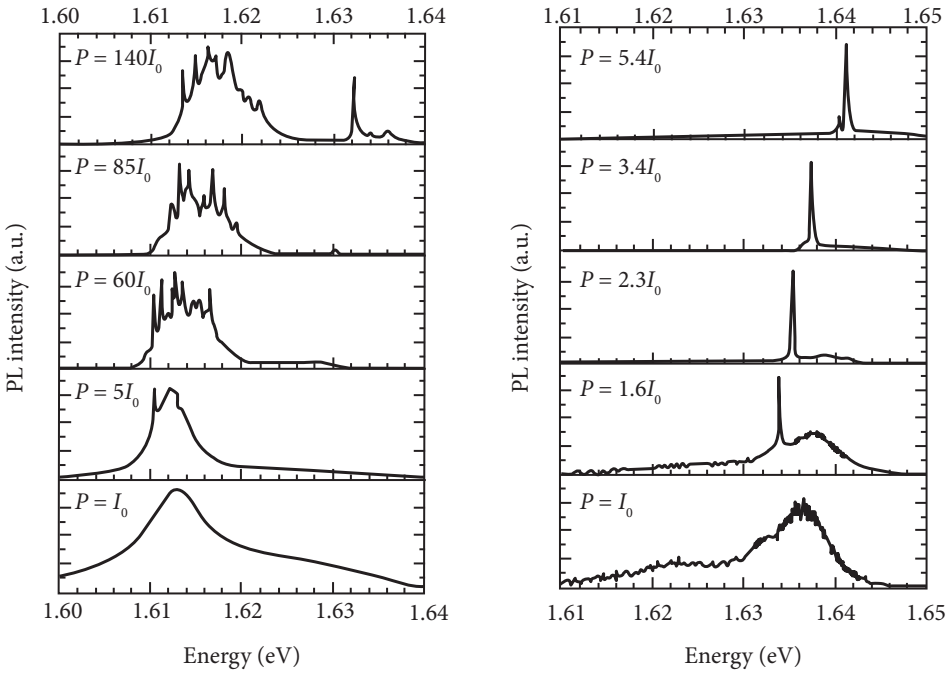

FIG. 1.5
PL spectra at 10 K of a disordered MAPI film (left panels) and microwire (right panels) as a function of the excitation intensity. Reproduced with permission Biccari, F. *et al.*, Mater. Today: Proc. **4**, S12–S18 (2017). Copyright 2017 Elsevier.

refractive index, can efficiently confine light enhancing its interaction with matter and, as a consequence, improving the light emission. From this point of view, HP nanoparticles (NPs) are under study as Mie resonators, which offer better advantages with respect to metal NPs traditionally used for plasmonic coupling but with higher losses. Recently, light-emitting nanoantennas were shown to possess a significant luminescence enhancement owing to the efficient coupling of excitons with the dipolar and multipolar Mie resonances (Tiguntseva *et al.*, 2018). The morphology of nanowires is such that they can act as Fabry–Perot microresonators guiding the light along the wire axis with a cavity quality factor as high as a few thousands (Eaton *et al.*, 2016). Nanoplates behave as microcavities sustaining the lasing action over a few transverse modes (Eaton *et al.*, 2016) and eventually in whispering gallery modes (Zhang *et al.*, 2016). From the definition of the quality factor of a cavity, $Q = f/\Delta f$, where f is the frequency of the mode and Δf is the broadening, given that the HPs of interest emit in the visible spectral range, it turns out that the Q-factor values of a few thousands correspond to line broadening of a few tenths of nanometers; better Q factors could be obtained by further reduction of the inhomogeneous broadening and cavity losses. Microcavity configurations have been considered to promote the exciton–cavity coupling; the Purcell effect at room temperature (Wang *et al.*, 2016) has been reported and wavelength-tunable excitonic lasing demonstrated (Wang *et al.*, 2018a). The strong

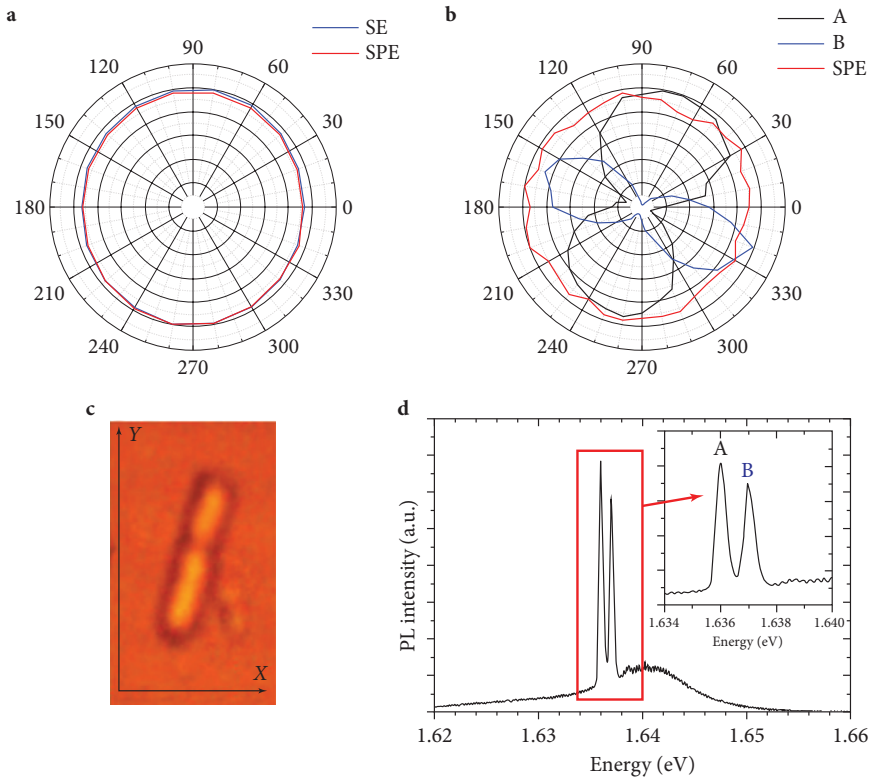

FIG. 1.6
(a) Polar diagram of the polarization of the spontaneous emission and the ASE for a MAPI spin-coated film. (b) Polar diagram of the polarization of A,B modes for a MAPI microwire sample. (c) Image of the microwire analyzed in panel (b). The polarizer at 0 is aligned along the *x*-axis. (d) Spectrum of the microwire in panel (c) showing the modes A,B whose polarization is reported in panel (b). Reproduced with permission Biccari, F. *et al.*, Mater. Today: Proc. **4**, S12–S18 (2017). Copyright 2017 Elsevier.

coupling regime was earlier explored and found for hybrid perovskites (Brehier *et al.*, 2006) with a Rabi splitting of 150 meV (at RT). Metallic halide perovskites have also been investigated for exciton–polariton lasers [for a complete review, see the work of Du *et al.* (2019)]. Nanowires have been explored acting themselves as microcavities (Du *et al.*, 2018), taking advantage of the high quality of the facets, which demonstrates the achievement of a strong coupling regime, as shown in Fig. 1.7.

A recent work (Guvenc *et al.*, 2020) has indicated the occurrence of a strong coupling between inorganic perovskite nanocrystals and plasmons when the nanocrystals are close to chemically functionalized metal films, which gives rise to a mixed mode plasmon–exciton. In all the previously mentioned cases, HPs demonstrate that higher performances can be obtained through cavity configuration, which has been studied for a long time with *traditional* semiconductors (i.e., arsenides, nitrides, selenides, etc.)

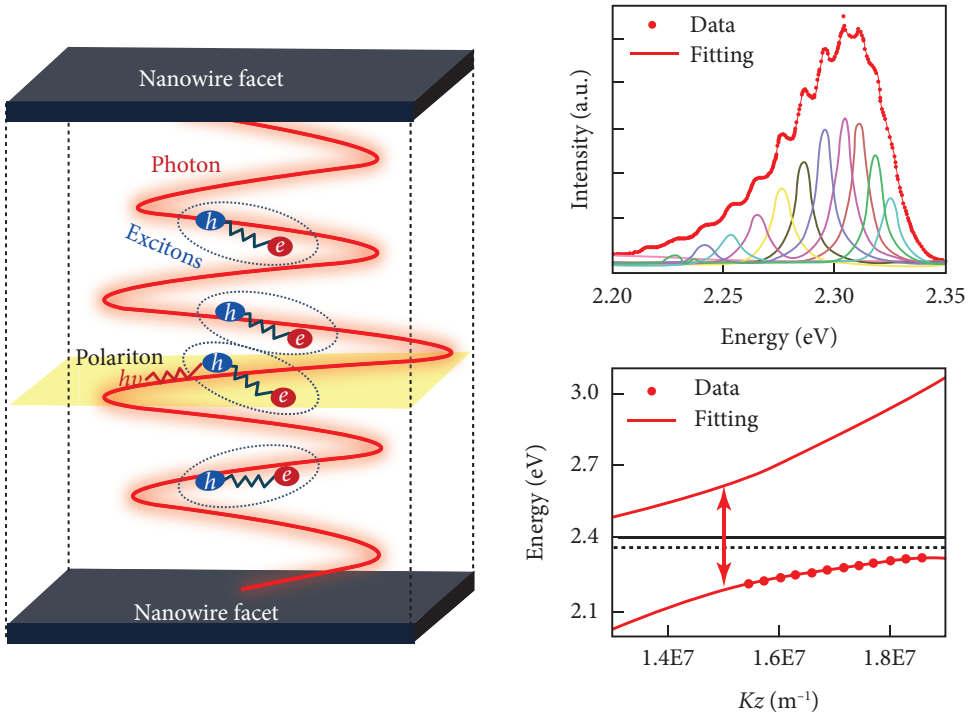

FIG. 1.7
Sketch of the exciton–photon coupling in a $CsPbBr_3$ nanowire, PL spectra of the same, and energy-wavevector dispersion curves along the nanowire axis. Adapted with permission from Du, W., Zhang, S., Shi, J. *et al.*, ACS Photonics **5**(5), 2051–2059 (2018). Copyright 2018 American Chemical Society.

in terms of mixed modes and radiative rate enhancement. Therefore, HPs have proven themselves as candidates for the development of efficient lasing sources and polariton lasing systems at RT. The achievement of a strong coupling regime with Rabi splitting of several tens/hundreds of meV allow for the exploration of exciton–polariton condensation at room temperature, which therefore provides the possibility to investigate the nonlinear regime in the condensate as developed in the microcavities of III–V and II–VI semiconductors at cryogenic temperatures.

1.3 HALIDE PEROVSKITES FOR PHOTONICS AND METAOPTICS

Both the commonly used solution-based synthesis/deposition techniques and the other procedures, such as chemical vapor deposition and sputtering, facilitate the integration of HP nanostructures and thin films in photonic cavities to manipulate the electric field properties in terms of polarization, field

distribution, etc. In fact, the synthesis/deposition techniques used for the preparation of HP thin films and nanostructures do not suffer from the limitation imposed by epitaxial growth when III–V and II–VI semiconductors are used as active materials in photonic crystal cavities. On one side, embedding HPs in photonic cavities can be an alternative route for the realization of efficient coherent laser sources with the control of the electromagnetic field properties, and on the other side, the deposition on photonic structures allows for the realization of metasurfaces and opens the route for the development of metaoptics. Very recently, significant advances have been reported concerning the realization of active metaoptics and dielectric nanophotonics using HP nanostructures as the active medium [see Berestennikov *et al.* (2019) and references therein]. As a newly born research field, impressive results have already been reported concerning the possibility of enhancing the photoluminescence in the presence of Mie resonances and at the same time, given the strong excitonic character of the emission, significant Fano resonances are expected at RT. The presence of Mie resonances for NPs deposited in a regular pattern on a surface allows for the realization of selective reflection and absorption by the metasurface which can also be realized in a dynamic way (Gao *et al.*, 2018). Broadband antireflective metasurfaces were recently realized (Dang *et al.*, 2020), which exhibited a strong suppression of the reflection ($<4\%$) and a spectrally broad transparency ($\sim 90\%$) region. Such results make possible the applications to multifunctional metadevices, in addition to the use in PV cells. Another relevant property that makes HPs of interest for metaoptics is the nonlinear response of this kind of material, which has been less explored until now. Outside of the linear regime, nonlinear optics based on HPs is a very recent and promising field (Xu *et al.*, 2020; and Zhou *et al.*, 2020). Despite their lattice centrosymmetric nature, second harmonic generation (SHG) is detected owing to the presence of ferroelectric domains; breaking of symmetry can also be induced by pressure and temperature, being thus related to the structural phase transitions characteristic of this class of materials. An in-depth discussion of harmonic generation can be found in the paper by Zhou *et al.* (2020). Moreover, in halide perovskites, efficient high-harmonic generation has been proven, which would be of extreme interest for photonic devices that operate in the attosecond timescale and for the realization of broadband light sources. Among the several kinds of nonlinearities, such as the mostly investigated harmonic generation (HG) and multiphoton absorption, it is worth noting that ultrafast light modulation by means of perovskite-based saturable absorbers already allows for the realization of stable mode-locked laser sources [see Xu *et al.* (2020) and references therein].

1.4 THEORETICAL TOOLS FOR ATOMISTIC DESCRIPTION OF THE MATERIAL PROPERTIES AND FOR THE ENHANCEMENT OF LIGHT ABSORPTION OF HP-BASED DEVICES

1.4.1 Finite-difference time-domain (FDTD) approaches

The area of modeling is becoming increasingly important for the mechanistic understanding and rational design of photonic nanostructures. Photonics has been revealed to be extremely suitable for

the computational approach because of the formal exactness of Maxwell's equations. Additionally, the relevant properties in photonics are not too small in the length scale making the *ab initio* simulation an excellent tool for supporting experiments and predicting novel features for nanofabrication techniques of photonic devices possessing a high degree of complexity.

In recent years, numerical techniques and algorithms have been developed to solve Maxwell's equations. Simulations of light scattering are of great help to understand the ideal size and distribution of NPs in the matrix. Such algorithms are exploitable in the study of electromagnetic photonic phenomena, with some limitations mainly associated with the dimensionality/size of the system under investigation. Three-dimensional space domains are characterized by massive computational costs, costs which become even higher once the simulations involve nonlinearities. In this numerical/computational scenario, two main approaches have emerged, one working in the time domain (TD), the other in the frequency domain (FD). The investigation of electromagnetic engineering systems has been influenced by the availability of computational resources with increasing performances. While indeed, at the very beginning, the main methods were based on numerical results obtained by infinite-series analytical solutions, later, the FD working setup has offered the possibility to obtain results about systems with higher complexity (Keller, 1962; and Kouyoumjian and Pathak, 1974). FD approaches show strong limitations in simulating the volumetric complexity and nonmetallic compositions of interest. Even more detrimental is the fact that in such approaches, the inclusion of device nonlinearities in the FD solutions to Maxwell's equation is a very cumbersome task that has motivated the search for alternative approaches to investigate electromagnetic engineering systems more efficiently. These challenges posed by the FD solution to Maxwell's equations were circumvented by the community after the seminal work of Yee who realized the advantages of a direct integration in the time domain and who first developed the so-called FDTD method (Yee, 1966). Driving forces that motivate the use of the FDTD method are the fact that no limitations in principle are present for the number of field unknowns that can be modeled and run as a consequence of a simplified integration compared with that of the frequency domain. It is indeed an explicit calculation that can easily treat nonlinearities of electromagnetic systems (Taflove and Hagness, 2005). The method originally fully exploits the time-dependent Maxwell's equations in an isotropic medium, which are (MKS units)

$$\frac{\partial \mathbf{B}}{\partial t} + \nabla \times \mathbf{E} = 0, \tag{1.1}$$

$$\frac{\partial \mathbf{D}}{\partial t} + \nabla \times \mathbf{H} = \mathbf{J}, \tag{1.2}$$

and

$$\mathbf{B} = \mu \mathbf{H} = \mu_r \mu_0 \mathbf{H}, \tag{1.3}$$

$$\mathbf{D} = \epsilon \mathbf{E} = \epsilon_r \epsilon_0 \mathbf{E}, \tag{1.4}$$

where **D** and **B** are the electric and magnetic flux, respectively; **E** and **H** the electric and magnetic field, respectively; and **J** is the electrical current density. Here, $\varepsilon(\mu)$, $\varepsilon_r(\mu_r)$, and $\varepsilon_0(\mu_0)$ are the electrical

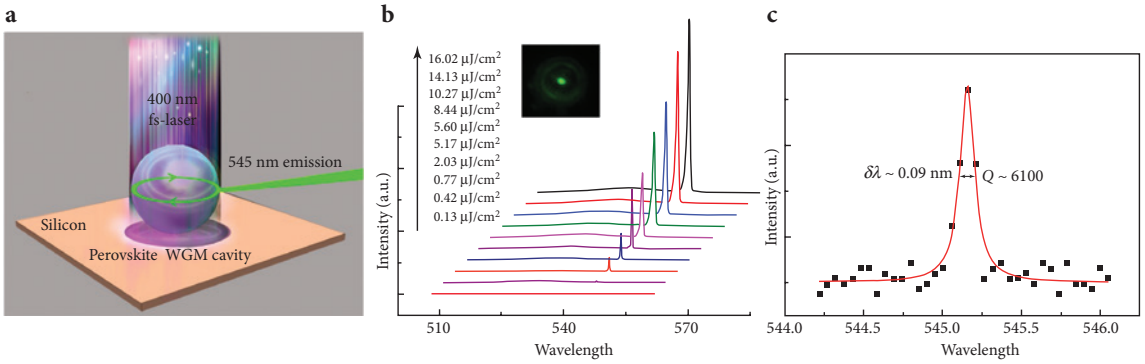

FIG. 1.8
(a) Schematic of an individual $CsPbBr_3$ microsphere on a silicon substrate. (b) Excitation power-dependent lasing spectra from one single $CsPbBr_3$ microsphere. (c) Lasing oscillation mode along with a Lorentzian fit with the indication of *Q*-factor. Adapted with permission Tang, B. *et al*., ACS Nano **11**(11), 10681–10688 (2017). Copyright 2017 American Chemical Society.

(magnetic) permittivity, the relative permittivity (permeability), and the free-space permittivity (permeability), respectively. The vector components in linear, isotropic, lossy, and nondispersive materials provide the six scalar equations, which are the bases of the FDTD algorithm that describes the interaction between the electric and magnetic fields with a 3D object:

$$\frac{\partial B_x}{\partial t} = \frac{\partial E_y}{\partial z} - \frac{\partial E_z}{\partial y}, \tag{1.5}$$

$$\frac{\partial B_y}{\partial t} = \frac{\partial E_z}{\partial x} - \frac{\partial E_x}{\partial z}, \tag{1.6}$$

$$\frac{\partial B_z}{\partial t} = \frac{\partial E_x}{\partial y} - \frac{\partial E_y}{\partial x}, \tag{1.7}$$

$$\frac{\partial D_x}{\partial t} = \frac{\partial H_z}{\partial y} - \frac{\partial H_y}{\partial z} - J_x, \tag{1.8}$$

$$\frac{\partial D_y}{\partial t} = \frac{\partial H_x}{\partial z} - \frac{\partial H_z}{\partial x} - J_y, \tag{1.9}$$

$$\frac{\partial D_z}{\partial t} = \frac{\partial H_y}{\partial x} - \frac{\partial H_x}{\partial y} - J_z. \tag{1.10}$$

Grid points for electric and magnetic fields (depicted in Fig. 1.9) are selected to properly satisfy a set of boundary conditions where, in a 3D space, every electric (magnetic) field component is surrounded by four magnetic (electric) components. The solution provided by Yee is a set of differential equations for Maxwell's equations, where (i, j, k) (in Fig. 1.9) correspond to $(i\Delta x, j\Delta y, k\Delta z)$ where i, j, and k are

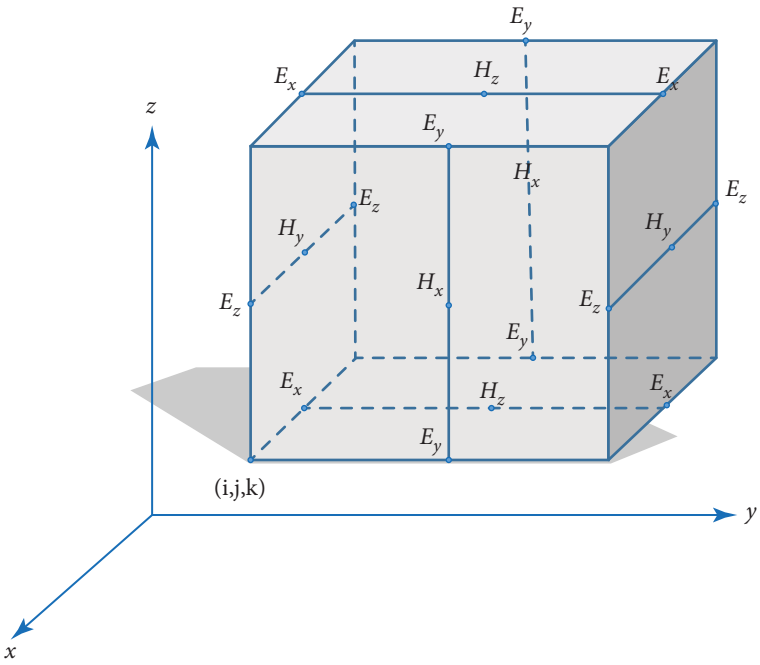

FIG. 1.9
Positions of electric and magnetic fields following the model of Yee (1966).

integers and Δs are increments along the three directions x, y, and z, respectively, and for any function of time and space, it is

$$F(n\Delta t, i\Delta x, j\Delta y, k\Delta z) = F^n(i,j,k). \tag{1.11}$$

The core of the approach of Yee is based on a few points that provide robustness to the algorithm. Electric and magnetic fields are solved in time and space by means of the coupling of Maxwell's equations, which offers a much improved result at variance with approaches based on the separated solution for the two fields. Concerning then the time propagation of the fields, the algorithm exploits the so-called leapfrog arrangement that allows for the self-consistent solution (at a selected time) of the magnetic field computations based on the previously calculated (and stored) data about the electric field. This somehow helps in saving computational time and also, according to the nature of the leapfrog arrangement, avoids issues related to simultaneous operations (no matrix inversion is required as in the case of the competing approach which is the finite element method) (Monk *et al.*, 2003).

The scattering problem in two dimensions describes the field components as formally independent from the z coordinate. In such a case, Maxwell's 2D equations will be decomposed into two independent

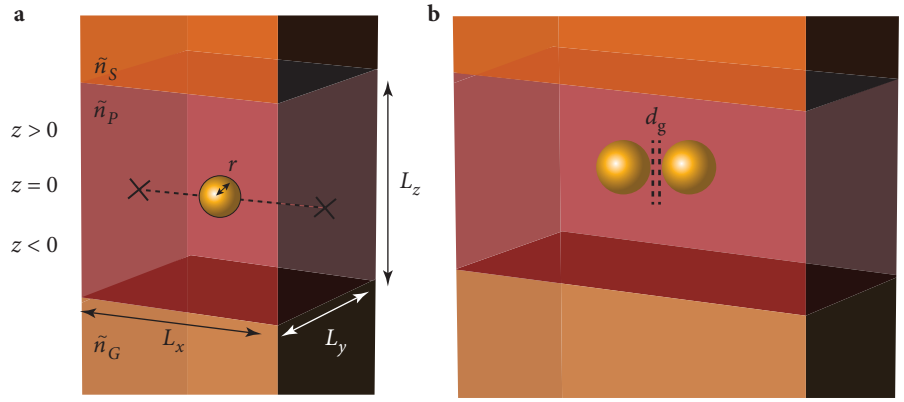

FIG. 1.10
(a) Schematics of a unit cell with dimensions $L_x \times L_y \times L_z$ of a glass–perovskite–spiro OMeTAD system, each layer characterized with refractive indexes, $\tilde{n}_{G(\omega)}$, $\tilde{n}_{P(\omega)}$, and $\tilde{n}_{s(\omega)}$, respectively, containing a gold nanoparticle (AuNP) of radius r centered at $(x,y,z = 0,0,0)$ nm. (b) Schematics of the same system as that in panel (a) containing two AuNPs with a gap distance d_g in a double volume $2(L_x \times L_y \times L_z)$. Reproduced with permission Carretero-Palacios, S. et al., H., J. Phys. Chem. C **119**(32), 18635–18640 (2015). Copyright 2015 American Chemical Society.

sets of equations, one called the transverse magnetic (TM) and the other the transverse electric (TE) mode, the latter propagating following (here $E_z = 0$, $H_x = H_y = 0$; $J = 0$)

$$-\mu\frac{\partial H_z}{\partial t} = \frac{\partial E_y}{\partial x} - \frac{\partial E_x}{\partial y},$$
$$\epsilon\frac{\partial H_z}{\partial y} = \frac{\partial E_z}{\partial t} \qquad -\frac{\partial H_z}{\partial x} = \epsilon\frac{\partial E_y}{\partial t}, \tag{1.12}$$

and the former (here $H_z = 0$, $E_x = E_y = 0$; $J = 0$)

$$\epsilon\frac{\partial E_z}{\partial t} = \frac{\partial H_y}{\partial x} - \frac{\partial H_x}{\partial y},$$
$$-\mu\frac{\partial H_x}{\partial t} = \frac{\partial E_z}{\partial y} \qquad \mu\frac{\partial H_y}{\partial t} = \epsilon\frac{\partial E_z}{\partial x}. \tag{1.13}$$

In the two sets of equations, there are no common field vector components, and they actually can exist without interactions and may describe totally different physical phenomena. While the TM mode can describe the electric field that is negligible at a metal surface (Taflove and Hagness, 2005), the TE mode can do the same for an electromagnetic field bound to the surface. For such modes, Yee (1966) has suggested a set of finite-difference equations that, once that proper field points are selected, can be applied and satisfy the boundary condition. The Yee approach still represents one of the most valid

and suitable approaches for the simulation of complex problems of electromagnetism. Nevertheless, further refinements have been suggested in the last two decades to the original formulation. These more refined algorithms allow one to circumvent issues associated with inhomogeneous media and complex geometries, which represent the critical points of the initially developed method, maintaining in this way a very high accuracy of the final electromagnetic simulation (Yefet and Petropoulos, 2001; Xie *et al.*, 2002; Cai and Deng, 2003; Hesthaven, 2003; and Zhao and Wei, 2004).

1.4.2 Density functional theory

As introduced, the photonics community aims to investigate the ways in which the electromagnetic fields work at the nanoscale by means of Maxwell's equation. However, quantum chemistry and condensed matter scientists try to determine the properties of molecules and solids at the atomic length scale by solving the many-body Schrödinger equation. Finding a solution for such an equation, even in its approximated forms (Born and Oppenheimer, 1927), has been a formidable challenge for theoreticians since its very first schemes provided by the Hartree–Fock method, with the biggest breakthrough resulting from the development of the density functional theory (DFT), the theoretical tool par excellence in modern condensed matter theory (Hohenberg and Kohn, 1964 and Kohn and Sham, 1965).

DFT has the fundamental merit of transforming the solution of a formally unsolvable electronic many-body problem into an easier, single-particle self-consistent one through a set of equations (Kohn *et al.*, 1996). Solids and molecules, i.e., systems where electrons and ions interact, are governed by the many-body Hamiltonian

$$\hat{\mathcal{H}} = \sum_{I=1}^{N_{ion}} -\frac{\nabla_I^2}{2} + \sum_{i=1}^{n_{elect}} -\frac{\nabla_i^2}{2} + \frac{1}{2}\sum_{I\neq J}\frac{Z_I Z_J}{|R_I - R_J|} + \frac{1}{2}\sum_{i\neq j}\frac{1}{|r_i - r_j|} + \sum_{i,I}\frac{-Z_i}{|r_i - R_I|}, \tag{1.14}$$

where the first two terms account for the kinetic energy of the ions and of the electrons, respectively, while the third, fourth, and last terms describe the ion–ion, electron–electron, and ion–electron interactions, respectively. This formalism would, in principle, provide the ground-state description of any state, but its complete solution is still not accessible, and it requires a substantial simplification.

The basic feature that characterizes the theory is, as introduced, the reduction of the system from an interacting nonsolvable electron description to a noninteracting one, which is solved by means of a set of equations (Kohn–Sham equations) that exploit an effective single-particle potential which includes the so-called exchange-correlation potential (V_{XC}), the core of the theory, where all the electron–electron interactions are stored. As the exact form of V_{XC} is unknown, approximations are required to solve it. The most representative ones are the local density (LDA) (Kohn and Sham, 1965) and generalized gradient (GGA) (Perdew and Wang, 1992 and Perdew *et al.*, 1996) approximations, the latter developed to correct the inaccuracies of the former (e.g., overbinding tendency).

The detailed description of the DFT features goes beyond the scope of the present contribution and, in this sense, we refer the readers to the plethora of reviews that have appeared in the literature in the last decades [see the works of Cohen *et al.* (2012); Becke (2014); and the references therein]. It is worth stressing that DFT is fundamental in studying the structural properties of molecules and solids; bond lengths, bond angles, as well as lattice parameters and the bulk modulus are only a few of the many observables that can be calculated by means of DFT, in the several flavors implemented in many computational codes, based both on plane waves [see the works of Kresse and Furthmüller (1996) and Giannozzi *et al.* (2009)] and on atomic orbitals [see the work of Soler *et al.* (2002)]. Although DFT, as implemented in the available computational codes, represents the most suitable tool for atomistic quantomechanical knowledge of any atomic/molecular/condensed phase system, its use for the description of a complex photonic setup remains quite cumbersome because of the object size, which usually is larger than that accessible to a bare DFT-based approach. Additionally, as DFT is a ground-state theory, it fails by construction in describing any excited-state properties, especially for semiconductors and insulators, yet it provides the best available starting point for excited-state property calculations (Onida *et al.*, 2002; and Manzhos *et al.*, 2021). Post-DFT methods, based on the use of both hybrid functionals and the Green function (GW), have been alternatively suggested. The former include an empirical fraction (often around 20%–25%) of Hartree–Fock exchange to correct the *bandgap issue* (Becke, 1993; and Heyd *et al.*, 2003) and the latter provides the exchange-correlation interaction integrating over the product between the Green function, $G(\mathbf{r}, \mathbf{r}', \varepsilon)$ and the screened Coulomb interaction $W(\mathbf{r}, \mathbf{r}', \varepsilon)$, and where the quasiparticle energies of the material are calculated from a perturbative expansion of the electron self-energies ($\sum$) and the dielectric function (ε) (Onida *et al.*, 2002). Recent years have witnessed the resurgence of halide perovskites as materials of great interest in optoelectronics and photonics, and accordingly, HPs have become a natural playground for DFT and post-DFT investigations [see the works of Even *et al.* (2013, 2014); Mosconi *et al.* (2013); Amat *et al.* (2014); Du (2014); Filippetti and Mattoni (2014); Giorgi *et al.* (2014); Haruyama *et al.* (2014, 2015, 2016); Yin *et al.* (2014); Stroppa *et al.* (2015); and Giorgi and Yamashita (2016, 2017)]. Thus, in Sec. 1.4.3, we review some representative papers that have recently appeared in the literature which exploit FDTD simulations and also papers that embody both FDTD simulations and DFT-based calculations in the study of the optoelectronic features of HPs. Owing to the very large number of papers appearing in the literature using FDTD approaches, we have to limit our discussion to focus on the different dimensionalities (from 3D to clusters), selecting few representative papers for each class.

1.4.3 Applications

In recent years, FDTD-related methodologies and numerical simulations have become almost a standard for the study of electromagnetic fields and, in view of its primary role in optoelectronics, halide perovskites have been accordingly extensively investigated in the time domain. Almost all dimensionalities have been studied by means of FDTD-based approaches (Rahman and Fobelets, 2015). Carretero-Palacios *et al.* (2015, 2016) applied the FDTD methodology to the analysis of absorption

enhancement in hybrid HP films with embedded Au NPs in the attempt to provide a guideline for the plasmonic applications of such devices. In the case of Au NPs dispersed in hybrid perovskites, Carretero-Palacios *et al.* (2015) mimicked a system where NPs are in the geometrical center of the perovskite film, similarly studying the effect of NP dispersion (dimers are also investigated) in the perovskite medium and in the range of wavelengths considered [see Figs. 1.11(a) and 1.11(b)].

For the film thickness considered, the inclusion of plasmonic Au NPs in thin hybrid layers of halide perovskites leads to an overall enhancement of perovskite sunlight absorption (from 6% to 12%). For a sphere radius of 60 nm (90 nm), a maximum integrated solar absorption increase of 10% (6%) is found for a perovskite film thickness of ∼200 nm (300 nm). Interestingly, for thin films, the formation of dimers is found to be beneficial, enhancing the absorption, an effect that vanishes

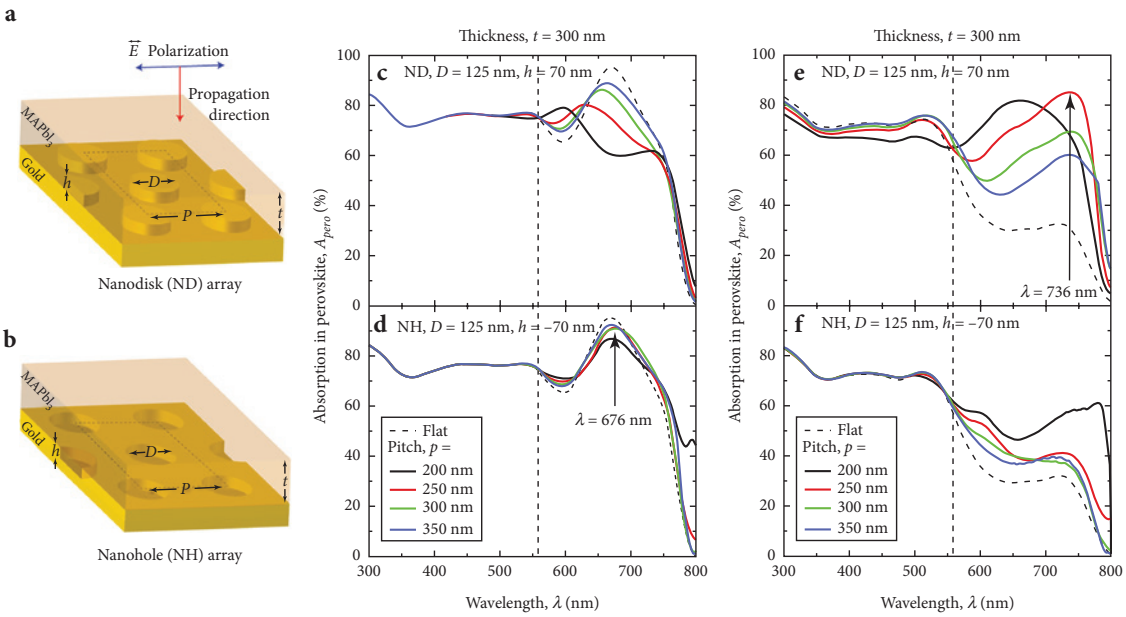

FIG. 1.11
(a and b) Schematic of simulated perovskite/gold geometries consisting of a perovskite ($MAPbI_3$) thin film on top of corrugated gold surfaces with an ND or NH array arranged in a hexagonal pattern. Here, D and h denote the diameter and height for the NDs or NHs, respectively; p represents the pitch of the hexagonal lattice; and t is the perovskite film thickness. The gold layer thickness is assumed to be semi-infinite. (c–f) Simulated absorption spectra in the perovskite film of thicknesses $t = 100$ and 300 nm for flat (dashed gray lines) and corrugated gold substrates (solid lines) with ND/NH diameter $D = 125$ nm and height $h = \pm 70$ nm. The pitch of the hexagonal pattern $p = 200$–350 nm. The vertical dashed line indicates $\lambda = 560$ nm, below which the transmitted light through the perovskite film is negligible owing to the large imaginary part of its refractive index. Reproduced with permission Shen, T. *et al.*, J. Phys. Chem. C **122**(41), 23691–23697 (2018). Copyright 2018 American Chemical Society.

for thicker films. Shen *et al.* (2018) investigated the plasmonic absorption enhancement in MAPI. The authors here calculated the photoconversion enhancement using simulated electric fields in perovskite films coated on top of both corrugated and flat Au surfaces with a hexagonal pattern of nanodisks and nanoholes. The simulated structure was here a simplified solar device [no contacts or carrier transport materials, see Figs. 1.11(c)–1.11(f)]. A planewave light source with wavelengths ranging between 300 and 800 nm was placed above the cell stack. Other geometrical parameters were varied (hole diameter, D; height of the hole, h; pitch of the waveguide, p; perovskite film thickness, t) and the relative results were collected. Such results revealed that the 100 nm-thick perovskite film on top of corrugated Au electrodes can be characterized by a PCE increase of ∼52% compared with the flat substrate (29.2% vs 19.2%). By simulating a perovskite thickness growth up to 150 nm and with a proper back contact, the device can show a PCE of 31.3%, a value that is close to that of a 400 nm-thick bulk-like device.

To achieve higher PCEs, novel device architectures have been recently suggested. Tandem devices formed by hybrid perovskites and silicon represent the latest frontier in this field (Bush *et al.*, 2017). Such architecture overcomes the issues associated with the single-junction technology mainly related to the conversion of photons with energy lower than the material bandgap and of charges excited by photons with energy higher than the bandgap that thermalize partly losing their energy. For such systems, Hossain *et al.* (2018) investigated the optical features by combining FDTD simulations with experimental measurements. The marked larger thickness of the tandem device compared to the wavelength of the incident light makes the simulation of the optical material properties quite cumbersome, thus requiring some experimentally measured data for the bottom cell. Accordingly, the authors mimicked the optical wave propagation in the top cell (consisting of ITO front contact, perovskite, ZnO back contact) and the coupling of light in the bottom solar cell. For the Si bottom cell (with infinite thickness and with surface texture), the quantum efficiency (QE) is calculated as the product between the transmission of the perovskite top cell and the QE of an experimentally reported single-junction solar device, while the QE of the top perovskite layer corresponds to its absorption (A). Results of such simulations performed by means of realistic input data predict a maximum energy conversion efficiency of 31.4% for Si/perovskite tandem devices, similarly claiming a potential increase of the open-circuit voltage of the top cell.

Tavakoli *et al.* (2015) investigated the optical features of flexible hybrid HP based solar devices assembled on ultrathin, robust, and transparent glasses. Films constituted by antireflection (AR) monocones were stuck on the front side of the glass with the purpose of enhancing the optical transmittance and reducing the moisture sensitivity of the device. Figure 1.12 shows the structure of the HP device investigated with particular focus on the structure of the polydimethylsiloxane (PDMS) cones attached to the surface of the front surface of the device. FDTD simulations were performed to support experimental data and the impact of the AR layer was investigated. Adding (removing) the AR layer had the effect of improving (reducing) absorption as shown by the absorption spectra and integrated absorption of perovskite thin film with nanocones integrated in the device shown in Fig. 1.13.

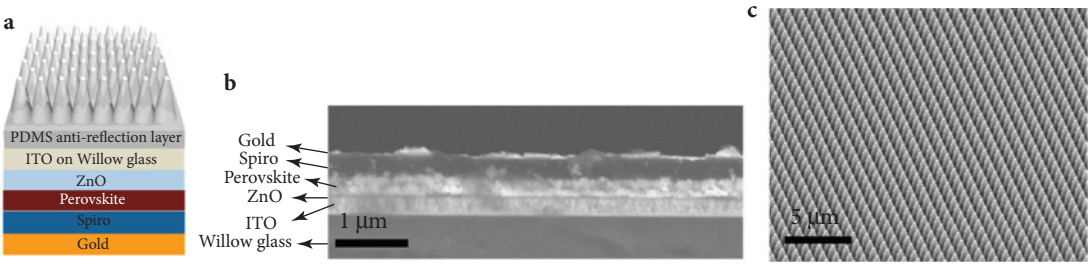

FIG. 1.12
(a) Schematic structure of the perovskite solar cell device with a nanocone PDMS film attached on the top. (b) SEM cross-sectional image of the perovskite solar cell based on a flexible glass substrate. (c) SEM image of PDMS nanocone with 1 μm pitch and 1 μm depth. Adapted with permission Tavakoli, M. M. *et al.*, ACS Nano **9**(10), 10287–10295 (2015). Copyright 2015 American Chemical Society.

The same group studied the possible implementation of $MAPbBr_3$ LEDs on nanophotonic substrates, obtaining an external quantum efficiency (EQE) of 17.5% (Zhang *et al.*, 2019a). This study is relevant as it offers a viable way to overcome the shortcomings (i.e., the light extraction) associated with the large refractive index difference existing among the materials forming the device. The optical modeling of the device was once more performed by means of FDTD simulations. The light extraction efficiency for several device geometries was calculated for the device consisting of seven layers, i.e., (i) the anodic

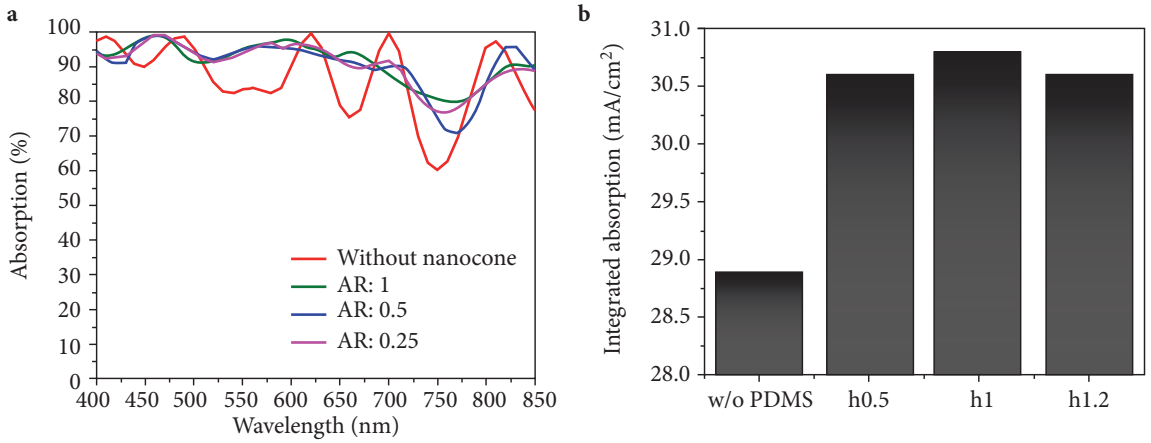

FIG. 1.13
FDTD simulation. (a) Absorption spectra and (b) integrated absorption of perovskite thin film integrated with nanocone PDMS films with different aspect ratios. Integrated absorption is calculated by integrating absorption spectra with an AM1.5G solar spectrum. Adapted with permission Tavakoli, M. M. *et al.*, ACS Nano **9**(10), 10287–10295 (2015). Copyright 2015 American Chemical Society.

alumina membranes (the real nanophotonic substrates consist of a layer of the nanodome array light coupler and a layer of nanowire array optical antennas), (ii) ITO, (iii) PEDOT:PSS, (iv) $MAPbBr_3$ layer, (v) F8 [poly(9,9-dioctylfluorene)], (vi) Ca, and (vii) Ag, in addition to the supporting substrate. The FDTD simulations revealed that by optimizing the nanophotonic structure, EQE values up to 73.7% were achievable, which stresses the relevance of such two-step light extraction (via nanodomes and nanowires) in improving the HP-based LED performances. Similarly, to improve the light harvesting of the HP layer, Tao *et al.* (2019) assembled and investigated an optical coupling structure with a double-decker inverted pyramid structure. As in the previous case, PDMS antireflection coatings with different light-trapping structures were integrated at the air–glass interface of the planar heterojunction device. The final layered structure was formed as follows: an Au layer (0.08 μm thick at the bottom), 2,2′,7,7′-tetrakis-9,9′-spirobifluorene (spiro-OMeTAD; 0.15 μm thick), MAPI (0.5 μm thick), TiO_2 (0.05 μm thick), FTO (0.286 μm thick), and the PDMS AR layer (5 μm thick), with the latter layer offering different (inverted pyramid, inverted circular cone, and inverted moth-eye structure) termination to the air. The FDTD simulations revealed that while light absorption increases (compared with the PDMS-free system) as a consequence of the three different micro–nano structures, the inverted pyramid was shown to maximize the AR property. The peculiar inverted-pyramid shape (with its high light-trapping effect) had the great advantage of enhancing light absorption of the HP layer. Integrating the double-decker inverted-pyramid geometry in the device may lead to HP-based solar devices that access massively higher photoconversion efficiencies.

Regardless of the different backgrounds of the two methodologies, interesting applications have exploited the combination of FDTD simulations and DFT calculations. Such combination has recently been proven to be useful for the study of HP optical features. In this context, Walters *et al.* (2020) combined FDTD and DFT to complement their experimental work that focused on directional emission from layered metal halide perovskites, nominally butylammonium-derived compounds ($BA_2MA_{n-1}Pb_nI_{3n+1}$, $n = 1, 2, 3$). In detail, DFT was employed (VandeVondele *et al.*, 2005) to calculate the (de)localization of the band edges in the layered systems and similarly the separation between carriers here interpreted as the exciton shape. However, by means of the FDTD approach, the LED emission efficiency was simulated. The device (see Fig. 1.14) was setup as stacked layers of different thicknesses of Al, LiF, electron transport material layer, perovskites, hole transport material layer, ITO, and glass (SiO_2) (each layer characterized by its own optical properties).

Out-coupling and maximum emission quantum efficiency were calculated. Maximum device efficiencies of 20%–30% were possible (isotropic), but with anisotropic emission, these numbers increased to nearly 30%–50%. Moving from $n = 1$ to $n = 3$, a similar increase in the efficiencies was observed, which was ascribed to the decreased reabsorption in the perovskite (Walters *et al.*, 2020), results that bear witness to the relevance of including emission anisotropy in photoluminescence quantum yield investigations of layered perovskites.

Still combining FDTD simulations and DFT calculations, Saffari *et al.* (2017), with a simple and effective approach, first characterized the structural and electronic properties of mixed Cl/I hybrid

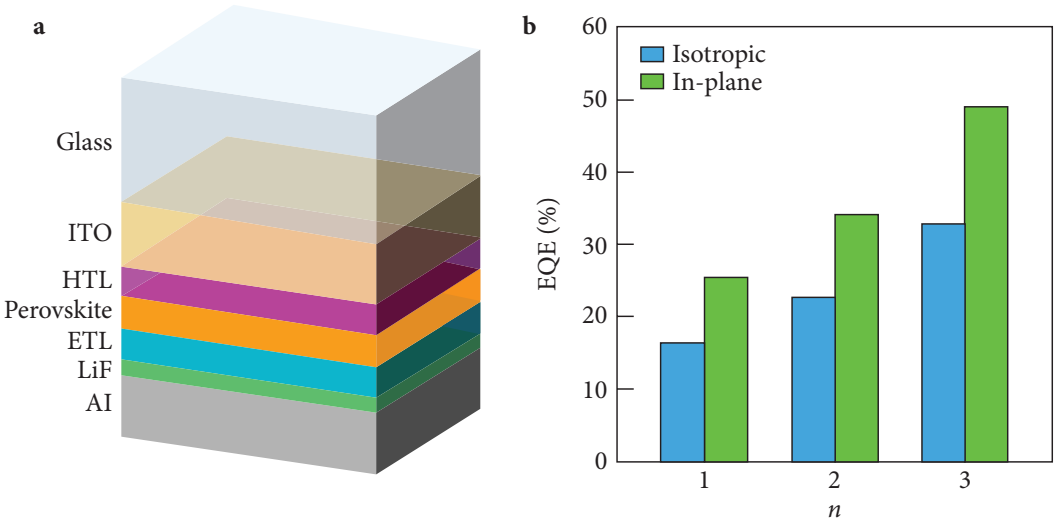

FIG. 1.14
Benefits of anisotropic emission for LEDs. (a) Thin-film layer stack representing a typical perovskite LED, which is used in FDTD optical simulations. (b) Simulated external quantum efficiency (EQE) for LED structures with iodide layered perovskite emitters having purely in-plane or isotropic transition dipole moment distributions. Unity photoluminescence quantum yield is assumed, and electrical losses are excluded. Reproduced with permission Walters, G. *et al.*, J. Phys. Chem. Lett. **11**(9), 3458–3465 (2020). Copyright 2020 American Chemical Society.

perovskites, nominally $CH_3NH_3PbI_{3-x}Cl_x$ ($x = 1, 2, 3$). FDTD analysis was performed using a five-layer device simulated as follows: a 350 nm-thick perovskite layer sandwiched between the two carrier transport materials, 15 and 10 nm thick, respectively, and finally the bottom layer acting as a metallic electrode constituted by Ag with 100 nm thickness. A 80 nm thick ITO layer is also used at the top of the cell. The combined results from the two approaches revealed that the addition of chlorine induces an increase in the bandgap (as from DFT), as well as a decrease in the lattice constants, refractive index, and extinction coefficient of the structure. In addition, using light-trapping techniques can result in a significant enhancement in the light absorption in these cells, up to 83.13%.

We have here reviewed some experimental technologies and theoretical methodologies applied to halide perovskites for photonic applications. Attention has been paid to light emission features and material nanostructuring, and to their impact in the experiments discussed within the chapter, while on the theoretical side, results of FDTD simulations are similarly discussed in view of the great potential of such methodology in predicting the optical features of photonic devices. Photonic applications of halide perovskites investigated by means of FDTD simulations and DFT calculations are finally reviewed.

REFERENCES

Amat, A. *et al.*, "Cation-induced band-gap tuning in organohalide perovskites: Interplay of spin–orbit coupling and octahedra tilting," Nano Lett. **14**(6), 3608–3616 (2014).

Baikie, T. *et al.*, "Synthesis and crystal chemistry of the hybrid perovskite $(CH_3NH_3)PbI_3$ for solid-state sensitised solar cell applications," J. Mater. Chem. A **1**(18), 5628–5641 (2013).

Becke, A. D., "A new mixing of Hartree–fock and local density-functional theories," J. Chem. Phys. **98**(2), 1372–1377 (1993).

Becke, A. D., "Perspective: Fifty years of density-functional theory in chemical physics," J. Chem. Phys. **140**(18), 18A301 (2014).

Berestennikov, A. S. *et al.*, "Active meta-optics and nanophotonics with halide perovskites," Appl. Phys. Rev. **6**(3), 031307 (2019).

Biccari, F. *et al.*, "Superlinear emission in bare perovskite: Amplified spontaneous emission in disordered film versus single crystal lasing," Mater. Today: Proc. **4**, S12–S18 (2017).

Born, M. and Oppenheimer, R., "Zur quantentheorie der molekeln," Ann. Phys. **389**(20), 457–484 (1927).

Borri, C. *et al.*, "First proof-of-principle of inorganic lead halide perovskites deposition by magnetron-sputtering," Nanomaterials **10**(1) (2020).

Brehier, A. *et al.*, "Strong exciton-photon coupling in a microcavity containing layered perovskite semiconductors," Appl. Phys. Lett. **89**(17), 171110 (2006).

Bush, K. A. *et al.*, "23.6%-efficient monolithic perovskite/silicon tandem solar cells with improved stability," Nat. Energy **2**(4), 1–7 (2017).

Cai, W. and Deng, S., "An upwinding embedded boundary method for Maxwell's equations in media with material interfaces: 2D case," J. Comput. Phys. **190**(1), 159–183 (2003).

Capasso, F., "Band-gap engineering: From physics and materials to new semiconductor devices," Science **235**(4785), 172–176 (1987).

Capper, P., Stuart, I., and Tim, J., "Epitaxial crystal growth: Methods and materials," in *Springer Handbook of Electronic and Photonic Materials*, edited by S. Kasap and P. Capper (Springer Nature Switzerland AG, 2017), pp. 1–1. ISBN: 978-3-319-48933-9

Carretero-Palacios, S., Calvo, M. E., and Míguez, H., "Absorption enhancement in organic–inorganic halide perovskite films with embedded plasmonic gold nanoparticles," J. Phys. Chem. C **119**(32), 18635–18640 (2015).

Carretero-Palacios, S., Jiménez-Solano, A., and Míguez, H., "Plasmonic nanoparticles as light-harvesting enhancers in perovskite solar cells: A user's guide," ACS Energy Lett. **1**(1), 323–331 (2016).

Chen, Q. *et al.*, "Under the spotlight: The organic-inorganic hybrid halide perovskite for optoelectronic applications," Nano. Today. **10**(3), 355–396 (2015).

Cohen, A. J., Mori-Sánchez, P., and Yang, W., "Challenges for density functional theory," Chem. Rev. **112**(1), 289–320 (2012).

Dang, N. H. M. *et al.*, "Tailoring dispersion of room-temperature exciton-polaritons with perovskite-based subwavelength metasurfaces," Nano Lett. **20**(3), 2113–2119 (2020).

De Marco, N. *et al.*, "Guanidinium: A route to enhanced carrier lifetime and open-circuit voltage in hybrid perovskite solar cells," Nano Lett. **16**(2), 1009–1016 (2016).

Du, M. H., "Efficient carrier transport in halide perovskites: Theoretical perspectives," J. Mater. Chem. A **2**(24), 9091–9098 (2014).

Du, W., Zhang, S., Shi, J. *et al.*, "Strong exciton-photon coupling and lasing behavior in All-inorganic $CsPbBr_3$ micro/nanowire Fabry-Pérot cavity," ACS Photonics **5**(5), 2051–2059 (2018).

Du, W., Zhang, S., Zhang, Q. *et al.*, "Recent progress of strong exciton-photon coupling in lead halide perovskites," Adv. Mater. **31**(45), 1804894 (2019). https://doi.org/10.1002/adma.201804894. eprint: https://onlinelibrary.wiley.com/doi/pdf/10.1002/adma.201804894

Eaton, S. W. *et al.*, "Lasing in robust cesium lead halide perovskite nanowires," Proc. Natl. Acad. Sci. U.S.A. **113**(8), 1993–1998 (2016).

Even, J. *et al.*, "Importance of spin–orbit coupling in hybrid organic/inorganic perovskites for photovoltaic applications," J. Phys. Chem. Lett. **4**(17), 2999–3005 (2013).

Even, J. *et al.*, "DFT and k·p modelling of the phase transitions of lead and tin halide perovskites for photovoltaic cells," Physica Status Solidi (RRL)–Rapid Res. Lett. **8**(1), 31–35 (2014).

Falsini, N. *et al.*, "Large-Area nanocrystalline caesium lead chloride thin films: A focus on the exciton recombination dynamics," Nanomaterials **11**(2) (2021). ISSN: 2079-4991.

Ferrando, A., Martinez Pastor, J. P., and Suarez, I., "Toward metal halide perovskite nonlinear photonics," J. Phys. Chem. Lett. **9**(18), 5612–5623 (2018).

Filippetti, A., and Mattoni, A., "Hybrid perovskites for photovoltaics: Insights from first principles," Phys. Rev. B **89**(12), 125203 (2014).

Furasova, A. D. *et al.*, "Resonant silicon nanoparticles for efficiency and stability enhancement of perovskite solar cells," J. Phys.: Conf. Ser. **1135**(1), 012067 (2018). IOP Publishing

Gao, Y. *et al.*, "Lead halide perovskite nanostructures for dynamic color display," ACS Nano **12**(9), 8847–8854 (2018).

Giannozzi, P. *et al.*, "QUANTUM ESPRESSO: A modular and open-source software project for quantum simulations of materials," J. Phys.: Condens. Matter **21**(39), 395502 (2009).

Giorgi, G., "Structural and electronic features of $Si/CH_3NH_3PbI_3$ interfaces with optoelectronic applicability: Insights from first-principles," Nano Energy **67**, 104166 (2020).

Giorgi, G. and Yamashita, K., "Zero-dipole molecular organic cations in mixed organic–inorganic halide perovskites: Possible chemical solution for the reported anomalous hysteresis in the current–voltage curve measurements," Nanotechnology **26**(44), 442001 (2015a).

Giorgi, G. and Yamashita, K., "Alternative, lead-free, hybrid organic–inorganic perovskites for solar applications: A DFT analysis," Chem. Lett. **44**(6), 826–828 (2015b).

Giorgi, G. and Yamashita, K., "Organic–inorganic halide perovskites: An ambipolar class of materials with enhanced photovoltaic performances," J. Mater. Chem. A **3**(17), 8981–8991 (2015c).

Giorgi, G. and Yamashita, K., "Zero-dimensional hybrid organic–inorganic halide perovskite modeling: Insights from first principles," J. Phys. Chem. Lett. **7**(5), 888–899 (2016).

Giorgi, G. and Yamashita, K., *Theoretical Modeling of Organohalide Perovskites for Photovoltaic Applications* (Taylor & Francis Group, 2017).

Giorgi, G., Fujisawa, J.-I. *et al.*, "Small photocarrier effective masses featuring ambipolar transport in methylammonium lead iodide perovskite: A density functional analysis," J. Phys. Chem. Lett. **4**(24), 4213–4216 (2013).

Giorgi, G., Fujisawa, J.-I. *et al.*, "Cation role in structural and electronic properties of 3D organic–inorganic halide perovskites: A DFT analysis," J. Phys. Chem. C **118**(23), 12176–12183 (2014).

Giorgi, G., Fujisawa, J.-I. *et al.*, "Organic–inorganic hybrid lead iodide perovskite featuring zero dipole moment guanidinium cations: A theoretical analysis," J. Phys. Chem. C **119**(9), 4694–4701 (2015).

Giorgi, G., Yamashita, K., and Palummo, M., "Two-dimensional optical excitations in the mixed-valence $Cs_2Au_2I_6$ fully inorganic double perovskite," J. Mater. Chem. C **6**(38), 10197–10201 (2018).

Gonzalez-Rodriguez, R. *et al.*, "Control of $CH_3NH_3PbI_3$ perovskite nanostructure formation through the Use of silicon nanotube templates," Small **12**(33), 4477–4480 (2016).

Guvenc, C. M., Polat, N., and Balci, S., "Strong plasmon-exciton coupling in colloidal halide perovskite nanocrystals near a metal film," J. Mater. Chem. C **8**(46), 16520–16526 (2020).

Haruyama, J. *et al.*, "Termination dependence of tetragonal $CH_3NH_3PbI_3$ surfaces for perovskite solar cells," J. Phys. Chem. Lett. **5**(16), 2903–2909 (2014).

Haruyama, J. *et al.*, "First-principles study of ion diffusion in perovskite solar cell sensitizers," J. Am. Chem. Soc. **137**(32), 10048–10051 (2015).

Haruyama, J. *et al.*, "Surface properties of $CH_3NH_3PbI_3$ for perovskite solar cells," Acc. Chem. Res. **49**(3), 554–561 (2016).

Heo, J. H. *et al.*, "Efficient inorganic–organic hybrid heterojunction solar cells containing perovskite compound and polymeric hole conductors," Nat. Photonics **7**(6), 486–491 (2013).

Hesthaven, J. S., "High-order accurate methods in time-domain computational electromagnetics: A review," Adv. Imaging Electron Phys. **127**, 59–123 (2003).

Heyd, J., Scuseria, G. E., and Ernzerhof, M., "Hybrid functionals based on a screened Coulomb potential," J. Chem. Phys. **118**(18), 8207–8215 (2003).

Hohenberg, P., and Kohn, W., "Inhomogeneous electron gas," Phys. Rev. **136**(3B), B864 (1964).

Hossain, M. I. *et al.*, "Nanophotonic design of perovskite/silicon tandem solar cells," J. Mater. Chem. A **6**(8), 3625–3633 (2018).

Huang, J. *et al.*, "Rich chemistry in inorganic halide perovskite nanostructures," Adv. Mater. **30**(48), 1802856 (2018).

Jena, A. K., Kulkarni, A., and Miyasaka, T., "Halide perovskite photovoltaics: Background, status, and future prospects," Chem. Rev. **119**(5), 3036–3103 (2019).

Jodlowski, A. D. *et al.*, "Large guanidinium cation mixed with methylammonium in lead iodide perovskites for 19% efficient solar cells," Nat. Energy **2**(12), 972–979 (2017).

Kang, J. and Wang, L.-W., "High defect tolerance in lead halide perovskite $CsPbBr_3$," J. Phys. Chem. Lett. **8**(2), 489–493 (2017).

Keller, J. B., "Geometrical theory of diffraction," J. Opt. SOC. Amer. **52**(2), 116–130 (1962).

Kohn, W. and Sham, L. J., "Self-consistent equations including exchange and correlation effects," Phys. Rev. **140**(4A), A1133 (1965).

Kohn, W., Becke, A. D., and Parr, R. G., "Density functional theory of electronic structure," J. Phys. Chem. **100**(31), 12974–12980 (1996).

Kojima, A. *et al.*, "Organometal halide perovskites as visible-light sensitizers for photovoltaic cells," J. Am. Chem. Soc. **131**(17), 6050–6051 (2009).

Kondo, S. *et al.*, "Room-temperature stimulated emission from microcrystalline $CsPbCl_3$ films," Appl. Phys. Lett. **87**(13), 131912 (2005).

Kouyoumjian, R. G., and Pathak, P. H., "A uniform geometrical theory of diffraction for an edge in a perfectly conducting surface," Proc. IEEE **62**(11), 1448–1461 (1974).

Kresse, G., and Furthmüller, J., "Efficient iterative schemes for ab initio total-energy calculations using a plane-wave basis set," Phys. Rev. B **54**(16), 11169 (1996).

Lee, M. M. *et al.*, "Efficient hybrid solar cells based on meso-superstructured organometal halide perovskites," Science **338**(6107), 643–647 (2012).

Li, G. *et al.*, "Highly efficient perovskite nanocrystal light-emitting diodes enabled by a universal crosslinking method," Adv. Mater. **28**(18), 3528–3534 (2016).

Liu, J. *et al.*, "Light-Induced self-assembly of cubic $CsPbBr_3$ perovskite nanocrystals into nanowires," Chem. Mater. **31**(17), 6642–6649 (2019).

Liu, Z. *et al.*, "Advances in inorganic and hybrid perovskites for miniaturized lasers," Nanophotonics. **9**(8), 2251–2272 (2020).

Makarov, S. *et al.*, "Halide-Perovskite resonant nanophotonics," Adv. Opt. Mater. **7**(1), 1800784 (2019).

Manzhos, S. *et al.*, "Materials design and optimization for next-generation solar cell and light-emitting technologies," J. Phys. Chem. Lett. **12**, 4638–4657 (2021).

Mitzi, D. B. *et al.*, "Conducting tin halides with a layered organic-based perovskite structure," Nature **369**(6480), 467–469 (1994).

Mitzi, D. B., "Synthesis, structure, and properties of organic-inorganic perovskites and related materials," Prog. Inorg. Chem. **48**, 1–121 (1999).

Mitzi, D. B., ""Templating and structural engineering in organic–inorganic perovskites," J. Chem. Soc., Dalton Trans. **1**, 1–12 (2001).

Møller, C. K., "A phase transition in cæsium plumbochloride," Nature **180**(4593), 981–982 (1957).

Møller, C. K., "Crystal structure and photoconductivity of caesium plumbohalides," Nature **182**(4647), 1436–1436 (1958).

Monk, P. *et al.*, *Finite Element Methods for Maxwell's Equations* (Oxford University Press, 2003).

Mosconi, E. *et al.*, "First-principles modeling of mixed halide organometal perovskites for photovoltaic applications," J. Phys. Chem. C **117**(27), 13902–13913 (2013).

Onida, G., Reining, L., and Rubio, A., "Electronic excitations: Density-functional versus many-body green's-function approaches," Rev. Mod. Phys. **74**(2), 601 (2002).

Palummo, M., Berrios, E. *et al.*, "Optical properties of lead-free double perovskites by ab initio excited-state methods," ACS Energy Lett. **5**(2), 457–463 (2020a).

Palummo, M., Varsano, D. *et al.*, "Halide Pb-free double–perovskites: Ternary vs. quaternary stoichiometry," Energies **13**(14), 3516 (2020b).

Perdew, J. P. and Wang, Y., "Accurate and simple analytic representation of the electron-gas correlation energy," Phys. Rev. B **45**(23), 13244 (1992).

Perdew, J. P., Burke, K., and Ernzerhof, M., "Generalized gradient approximation made simple," Phys. Rev. Lett. **77**(18), 3865 (1996).

Protesescu, L. *et al.*, "Nanocrystals of cesium lead halide perovskites ($CsPbX_3$, X = Cl, Br, and I): Novel optoelectronic materials showing bright emission with wide color gamut," Nano Lett. **15**(6), 3692–3696 (2015).

Rahman, T. and Fobelets, K., "Efficient tool flow for 3D photovoltaic modelling," Comp. Phys. Commun. **193**, 124–130 (2015).

Rocks, C. *et al.*, "Type-I alignment in $MAPbI_3$ based solar devices with doped-silicon nanocrystals," Nano Energy **50**, 245–255 (2018). ISSN: 2211–2855. https://doi.org/10.1016/j.nanoen.2018.05.036

Saffari, M. *et al.*, "DFT analysis and FDTD simulation of $CH_3NH_3PbI_{3-x}Cl_x$ mixed halide perovskite solar cells: Role of halide mixing and light trapping technique," J. Phys. D: Appl. Phys. **50**(41), 415501 (2017).

Schönemann, S. *et al.*, "Halide perovskite 3D photonic crystals for distributed feedback lasers," ACS Photonics **4**(10), 2522–2528 (2017).

Shen, T., Siontas, S., and Pacifici, D., "Plasmon-enhanced thin-film perovskite solar cells," J. Phys. Chem. C **122**(41), 23691–23697 (2018).

Shi, J., Wang, Y., and Zhao, Y., "Inorganic $CsPbI_3$ perovskites toward high-efficiency photovoltaics," Energy Environ. Mater. **2**(2), 73–78 (2019). Eprint: https://onlinelibrary.wiley.com/doi/pdf/10.1002/eem2.12039

Slavney, A. H. *et al.*, "A bismuth-halide double perovskite with long carrier recombination lifetime for photovoltaic applications," J. Am. Chem. Soc **138**(7), 2138–2141 (2016).

Soler, J. M. *et al.*, "The SIESTA method for ab initio order-N materials simulation," J. Phys.: Condens. Matter **14**(11), 2745 (2002).

Song, J. *et al.*, "Quantum dot light-emitting diodes based on inorganic perovskite cesium lead halides ($CsPbX_3$)," Adv. Mater. **27**(44), 7162–7167 (2015).

Stranks, S. D. *et al.*, "Electron-hole diffusion lengths exceeding 1 micrometer in an organometal trihalide perovskite absorber," Science **342**(6156), 341–344 (2013).

Stroppa, A. *et al.*, "Ferroelectric polarization of $CH_3NH_3PbI_3$: A detailed study based on density functional theory and symmetry mode analysis," J. Phys. Chem. Lett. **6**(12), 2223–2231 (2015).

Su, R. *et al.*, "Room-temperature polariton lasing in all-inorganic perovskite nanoplatelets," Nano Lett. **17**(6), 3982–3988 (2017).

Sutherland, B. R. and Sargent, E. H., "Perovskite photonic sources," Nat. Photonics **10**(5), 295–302 (2016).

Taflove, A. and Hagness, S. C., *Computational Electrodynamics: The Finite-Difference Time-Domain Method*, (Artech House, Boston/London, 2005).

Tang, B. *et al.*, "Single-mode lasers based on cesium lead halide perovskite submicron spheres," ACS Nano **11**(11), 10681–10688 (2017).

Tao, H. *et al.*, "High absorption perovskite solar cell with optical coupling structure," Opt. Commun. **443**, 262–267 (2019).

Tavakoli, M. M. *et al.*, "Highly efficient flexible perovskite solar cells with antireflection and self-cleaning nanostructures," ACS Nano **9**(10), 10287–10295 (2015).

Tiguntseva, E. *et al.*, "Resonant silicon nanoparticles for enhancement of light absorption and photoluminescence from hybrid perovskite films and metasurfaces," Nanoscale **9**(34), 12486–12493 (2017).

Tiguntseva, E. Y. *et al.*, "Light-Emitting halide perovskite nanoantennas," Nano Lett. **18**(2), 1185–1190 (2018).

Tong, Y. *et al.*, "Spontaneous self-assembly of perovskite nanocrystals into electronically coupled supercrystals: Toward filling the green Gap," Adv. Mater. **30**(29), 1801117 (2018).

VandeVondele, J. *et al.*, "Quickstep: Fast and accurate density functional calculations using a mixed Gaussian and plane waves approach," Comput. Phys. Commun. **167**(2), 103–128 (2005).

Volonakis, G. *et al.*, "$Cs_2InAgCl_6$: A new lead-free halide double perovskite with direct band gap," J. Phys. Chem. Lett. **8**(4), 772–778 (2017).

Walters, G. *et al.*, "Directional light emission from layered metal halide perovskite crystals," J. Phys. Chem. Lett. **11**(9), 3458–3465 (2020).

Wang, J., Cao, R. *et al.*, "Purcell effect in an organic-inorganic halide perovskite semiconductor microcavity system," Appl. Phys. Lett. **108**(2), 022103 (2016).

Wang, J., Da, P. *et al.*, "Lasing from lead halide perovskite semiconductor microcavity system," Nanoscale **10**(22), 10371–10376 (2018a).

Wells, H. L., "Über die cäsium-und kalium-bleihalogenide," Zeitschrift für anorganische Chemie **3**(1), 195–210 (1893).

Wu, C. *et al.*, "The Dawn of lead-free perovskite solar cell: Highly stable double perovskite $Cs_2AgBiBr_6$ film," Adv. Sci. **5**(3), 1700759 (2018).

Wu, S. *et al.*, "Efficient large guanidinium mixed perovskite solar cells with enhanced photovoltage and low energy losses," Chem. Commun. **55**(30), 4315–4318 (2019).

Xie, Z., Chan, C.-H., and Zhang, B., "An explicit fourth-order staggered finite-difference time-domain method for Maxwell's equations," J. Comput. Appl. Math. **147**(1), 75–98 (2002).

Xing, G., Mathews, N., Sun, S. *et al.*, "Long-range balanced electron-and hole-transport lengths in organic-inorganic $CH_3NH_3PbI_3$," Science **342**(6156), 344–347 (2013).

Xing, G., Nripan, M., Swee, S. L. *et al.*, "Low-temperature solution-processed wavelength-tunable perovskites for lasing," Nat. Mater. **13**(5), 476–480 (2014).

Xu, J. *et al.*, "Halide perovskites for nonlinear optics," Adv. Mater. **32**(3), 1806736 (2020).

Yao, E.-P. *et al.*, "High-Brightness blue and white LEDs based on inorganic perovskite nanocrystals and their composites," Adv. Mater. **29**(23), 1606859 (2017).

Yee, K., "Numerical solution of initial boundary value problems involving Maxwell's equations in isotropic media," IEEE Trans. Antennas Propag. **14**(3), 302–307 (1966).

Yefet, A., and Petropoulos, P. G., "A staggered fourth-order accurate explicit finite difference scheme for the time-domain Maxwell's equations," J. Comput. Phys. **168**(2), 286–315 (2001).

Yin, W.-J., Shi, T., and Yan, Y., "Unusual defect physics in $CH_3NH_3PbI_3$ perovskite solar cell absorber," Appl. Phys. Lett. **104**(6), 063903 (2014).

Yoon, H. C. *et al.*, "Study of perovskite QD down-converted LEDs and Six-color white LEDs for future displays with excellent color performance," ACS Appl. Mater. Interface **8**(28), 18189–18200 (2016).

Zhang, Q. *et al.*, "High-Quality whispering-gallery-mode lasing from cesium lead halide perovskite nanoplatelets," Adv. Funct. Mater. **26**(34), 6238–6245 (2016). Eprint: https://onlinelibrary.wiley.com/doi/pdf/10.1002/adfm.201601690

Zhang, L. *et al.*, "Ultra-bright and highly efficient inorganic based perovskite light-emitting diodes," Nat. Commun. **8**(1), 1–8 (2017).

Zhang, Q. *et al.*, "Efficient metal halide perovskite light-emitting diodes with significantly improved light extraction on nanophotonic substrates," Nat. Commun. **10**(1), 1–9 (2019a).

Zhang, Y. *et al.*, "Photonics and optoelectronics using nano-structured hybrid perovskite media and their optical cavities," Phys. Rep. **795**, 1–51 (2019b).

Zhao, S., and Wei, G. W., "High-order FDTD methods via derivative matching for Maxwell's equations with material interfaces," J. Comput. Phys. **200**(1), 60–103 (2004).

Zhao, Y. *et al.*, "Research progress in large-area perovskite solar cells," Photon. Res. **8**(7), A1–A15 (2020).

Zhou, Y. *et al.*, "Nonlinear optical properties of halide perovskites and their applications," Appl. Phys. Rev. **7**(4), 041313 (2020).

Zhu, H. *et al.*, "Lead halide perovskite nanowire lasers with low lasing thresholds and high quality factors," Nat. Mater. **14**(6), 636–642 (2015).